On an Antenna Design for 2D Scalar Near-Field Microwave Tomography

Nozhan Bayat and Puyan Mojabi

Department of Electrical and Computer Engineering
University of Manitoba, Winnipeg, MB, R3T 5V6, Canada
Bayatn@myumanitoba.ca, Puyan.Mojabi@UManitoba.ca

Abstract ― Some desired antenna specifications for performing two-dimensional (2D) transverse magnetic (TM) microwave tomography imaging are presented and discussed. These desired specifications are governed by the need to reduce the discrepancy between the 3D measurement configuration and the utilized 2D TM inversion algorithm, as well as the desire to enhance the achievable image accuracy and resolution. Driven by these specifications, an existing compact ultrawideband antenna element is modified. These modifications attempt to make the near-field distribution of this antenna more focused in the two orthogonal planes in the forward near-field zone of the antenna, while keeping its physical size relatively small and maintaining multiple frequencies of operation for this antenna. The final antenna has a physical size of 26×29×38.5 mm^3 and can operate at two different frequency bands (2.34-5.04 GHz and 8.06-13 GHz based on the $|S_{11}| \leq$ -8 dB impedance bandwidth definition). The measured near-field distribution of this antenna is presented in the imaging plane and the plane perpendicular to the imaging plane.

Index Terms ― Antenna design and measurements, microwave tomography, near-field zone.

I. INTRODUCTION

Microwave tomography (MWT) is a non-ionizing imaging technique that uses microwave scattering measurements collected outside the object of interest (OI) to create quantitative images from the relative permittivity and conductivity profiles of the OI. These two quantitative images can then be used for several applications including industrial non-destructive evaluation and biomedical diagnosis [1-3]. Creating MWT images requires performing at least two steps. In the first step, the data collection step, the OI is successively irradiated by some antennas. The resulting scattered fields emanating from the OI are then collected at some receiving antennas. The second step, usually referred to as the inversion step, attempts to reconstruct the dielectric profile of the OI from this measured scattered data by solving the associated electromagnetic inverse scattering problem. These two steps are interlinked; the antenna and hardware design need to be performed in such a way to support the assumptions made in the development of the utilized inversion algorithm. Any discrepancies between the actual measurement and computational model configurations result in the so-called modeling error [4]; thus, degrading the achievable image resolution and accuracy. The link between the inversion algorithm and the required antenna specifications for the so-called 2D TM near-field MWT systems will be discussed in Section II.

2D TM near-field MWT systems, e.g., see [5-7], are the most common form of MWT systems. In such systems, the inversion algorithm assumes a 2D imaging domain, located in the *x-y* plane, which is irradiated by an electric field perpendicular to the imaging domain, E_z. 2D TM near-field systems offer ease of system and algorithm implementation, and can also provide a reasonable balance between the number of unknowns to be reconstructed and the number of measured data points [8, Section 1.4.1]. However, the main disadvantage of these MWT systems lies in performing 2D TM inversion on microwave scattering data collected in a 3D scattering environment, thus, suffering from the modeling error. One way to mitigate these 3D effects in the 2D inversion using an appropriate antenna near-field distribution is discussed in Section II.

This paper starts with attempting to establish a relation between the assumptions made in 2D TM inversion algorithms and preferable antenna specifications for such systems. We then consider some other preferable antenna specifications that can result in further enhancement of the achievable resolution and accuracy. Based on these specifications, an existing antenna element is modified and fabricated. The measurement results and a final discussion will then be presented. Finally, we note that the materials of this paper have been taken from the M.Sc. thesis of the first author [8]. A one-page abstract of this work was also presented by the authors in [9].

II. FROM 2D TM NUMERICAL MODEL TO ANTENNA DESIGN SPECIFICATIONS

Let's consider the full-wave MWT formulation as

Submitted On: October 1, 2014
Accepted On: April 20, 2015

presented in [10]:

$$\nabla^2 \boldsymbol{E} + \omega^2 \varepsilon\mu \boldsymbol{E} + \nabla(\boldsymbol{E}.\nabla\varepsilon/\varepsilon) = -\mathrm{j}\omega\mu \boldsymbol{J}, \quad (1)$$

where ∇^2 is the Laplacian operator and ∇ represents the gradient operator. The vector $\boldsymbol{E}$ represents the vectorial electric field having three components in the Cartesian coordinate. The current source term is denoted by $\boldsymbol{J}$, and the inhomogeneous complex permittivity profile is denoted by ε. As noted in [10], the third term on the left side of (1) couples the three components of the electric field vector together. On the other hand, a 2D TM inversion algorithm assumes that the wave propagation is represented by the following scalar equation:

$$\nabla^2 E_z + \omega^2 \varepsilon\mu E_z = -\mathrm{j}\omega\mu J_z, \quad (2)$$

where E_z and J_z are the $\hat{z}$ components of $\boldsymbol{E}$ and $\boldsymbol{J}$ respectively. Any discrepancies between the full-wave formulation of (1), and the scalar wave equation of (2) can be regarded as the modelling error in the 2D TM MWT problem. To minimize this discrepancy, the $\hat{z}$ contribution of the third term on the left side of (1) needs to be as small as possible. That is,

$$\frac{\partial}{\partial z}\left(\frac{\frac{\partial\varepsilon}{\partial x}E_x+\frac{\partial\varepsilon}{\partial y}E_y+\frac{\partial\varepsilon}{\partial z}E_z}{\varepsilon}\right) \to 0. \quad (3)$$

Note that the variations of the complex permittivity profile with respect to x and y are to be imaged; thus, it cannot be assumed that $\frac{\partial\varepsilon}{\partial x}$ and $\frac{\partial\varepsilon}{\partial y}$ are very small. Also, E_z is the electric field vector used in 2D TM inversion; thus, this component cannot be assumed to be small either. Therefore, we may enforce (3) by making E_x, E_y, and $\frac{\partial\varepsilon}{\partial z}$ very small.

In practical applications, we have no control over $\frac{\partial\varepsilon}{\partial z}$. Therefore, to reduce the effect of this quantity, we speculate that if the antenna has a focused near-field distribution in a plane perpendicular to the imaging domain, the antenna will have limited solid angle view along the z direction. As a result, the variation of the permittivity profile along the z direction will be less "seen" by the antenna, thus, effectively reducing the contribution of $\frac{\partial\varepsilon}{\partial z}$. Therefore, the near-field focusing on a plane perpendicular to the imaging domain will serve as our first requirement to mitigate the 3D effects. Also, as noted earlier, we need to ensure that E_x and E_y of the antenna are sufficiently small. This will serve as our second requirement to alleviate the 3D effects.

Using numerical studies, we have recently shown that the MWT quantitative accuracy and resolution can be enhanced by using appropriate antenna incident field distributions [8,11,12]. In particular, in [8,11,12], we have shown that the use of an antenna with a focused near-field distribution can enhance the achievable resolution and accuracy from MWT. To this end, we are interested in designing an antenna whose near-field distribution is sufficiently focused within the imaging plane. Note that our first requirement was concerned with focusing in a plane perpendicular to the imaging domain; however, this new third requirement is concerned with focusing within the imaging domain. Also, note that the studies in [8,11,12] assume that we have sufficient number of antennas around the OI; otherwise, having few wide angle illuminations can be more useful than few focused illuminations.

It has also been shown that enhanced MWT reconstruction can be obtained by the use of multiple-frequency data sets [13]. To this end, we have another requirement: the antenna element should operate at multiple frequencies. Also, the bandwidth around each frequency should not be too narrow as the resonance frequencies might shift due to mutual coupling and fabrication inaccuracy [14]. In addition, in MWT, the number of required measured data points to reconstruct an OI is dependent on the OI itself. Since the OI is the unknown of the problem, the general strategy is to collect as much data as possible. Therefore, another requirement will be for the size of the antenna to be sufficiently small so as to accommodate several co-resident antennas in the data collection system. Finally, from a numerical point of view, it is desired that the antenna can be modeled in the inversion algorithm [15]. Satisfying all these criteria simultaneously may not be possible; thus, a trade-off between these different criteria is often sought.

III. DESIGN PROCEDURE

We consider an existing antenna as reported in [16]. This monopole-like slot antenna already satisfies two of the criteria: it is ultrawideband (UWB), and is reasonably small (26×29 mm^2). To accommodate the other criteria, we start by attempting to increase its near-field focusing in two orthogonal planes, one of which is the imaging plane. We then discuss how these modifications affect the other required criteria. As noted earlier, we consider near-field MWT in which the imaging domain resides in the radiating near-field zone of the antenna. Thus, we avoid using far-field terms such as "pattern", "polarization", etc. Instead, we use "field distribution", "E_x and E_y compared to E_z", etc.

The initial antenna, which is a monopole-like slot antenna as reported in [16], was modeled in the ANSYS HFSS software as shown in Fig. 1 (a). (This figure shows the initial antenna after performing some geometrical optimizations; thus, some of its dimensions differ from that reported in [16].) As can be seen in this figure, we have chosen a Cartesian coordinate system in such a way that the top surface of the antenna lies within the y-z plane. This antenna is fed by a fork-shaped coplanar waveguide structure, which is itself fed by a 50 Ω coaxial cable. Also, this antenna is linearly polarized. Although polarization of an antenna is a far-field quantity, and we are concerned with near-field MWT, it was speculated that starting with a linearly polarized antenna may correspond to a more dominant E_z as compared to E_x and

E_y, thus, helping satisfy (3).

We then considered the fact that the final antenna eventually needs to be used in an actual MWT system. Therefore, the backward radiation of the antenna needs to be minimized so as to reduce non-desired reflections from the feeding cables and the MWT enclosure. To this end, we employed the idea of using a metallic cavity that was presented in [17]. This metallic cavity, which is an open box below the monopole-like slot antenna, can be best seen in Fig. 4 [left], which shows the fabricated antenna. Having seen the fabricated cavity, Fig. 1 (b), which shows this cavity in the HFSS software, can now be better understood. However, as opposed to [17], we do not use radio frequency absorbers to fill the space between the metallic cavity and the antenna. Initially, we chose to not do that so as to increase the efficiency of the final antenna element. However, we later speculated that we might be able to use the reflection of the metallic cavity to strengthen the near-field focusing in the forward direction of the antenna. (This will be explained later in more details.) Therefore, we chose to not include any absorbers between the metallic cavity and the slot antenna. This resulted in two different issues. First, the resulting antenna lost its UWB properties. At this point, we optimized the antenna using the HFSS software so as to improve its bandwidth. This improved bandwidth did not make the antenna UWB, but resulted in an antenna supporting multiple frequencies of operation. Styrofoam was then used to hold the cavity and antenna together. This can be best seen by looking at the space below the fabricated antenna in Fig. 4 [left].

Based on a recent work on a Vivaldi antenna for radar-based microwave imaging applications [18], we then added a dielectric superstrate to the antenna so as to make its near-field distribution more focused. To this end, we chose a piece of RT/duroid 6010 that has a relative permittivity of $\varepsilon_r = 10.2$, and a loss tangent of $tan\,\delta = 0.0023$. (The standard thickness of this dielectric material is 1.9 mm. This thickness was thus chosen.) It was speculated that this dielectric material is appropriate since it has a larger permittivity as compared to the antenna FR4 substrate; thus, tending to keep the electric field distribution around itself, and helping toward near-field focusing. We also decided to choose the surface area of this superstrate to be a rectangle covering the slot of the antenna, as shown in Fig. 1 (b). To find an appropriate separation between this superstrate and the antenna, the impedance bandwidth was optimized over several slot and feeding parameters as well as the separation between the superstrate and the slot.

At this point, we noticed that the near-field distribution of the antenna toward the $\hat{x}$ direction becomes more focused due to the presence of this superstrate. Based on this observation, we decided to focus the near-field distribution of the antenna in the negative $\hat{x}$ direction using the same technique with the hope that this focused near-field distribution might be reflected back by the metallic cavity toward the forward direction of the antenna, thus, strengthening the effect of the focused near-field distribution in the $\hat{x}$ direction. To this end, we placed the same RT/duroid 6010 dielectric material between the slot and the cavity; see Fig. 4 [right] and Fig. 2. This dielectric was placed below the antenna, and directly beneath the superstrate. To find an appropriate separation between this dielectric and the slot, the impedance bandwidth of the antenna was optimized over several parameters including the separation the superstrate from the slot.

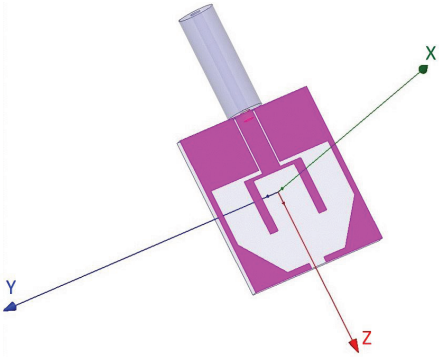

(a) Monopole-like slot antenna (see [16])

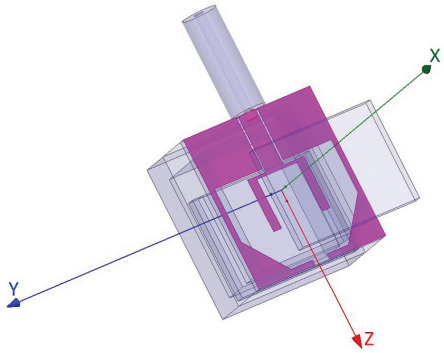

(b) Covered monopole-like slot antenna

Fig. 1. (a) Monopole-like slot antenna on a FR4 PCB with a thickness of h=1.55 mm (see [16]), and (b) covered monopole-like slot antenna. The covered monopole-like slot antenna uses a metallic cavity and a superstrate as well as a dielectric material between the slot and the metallic cavity.

This concludes our design procedure. The final antenna is shown in Fig. 4 [right]. As can be seen, the whole antenna is covered in a styrofoam box with three openings, the middle one to fit the monopole-like slot antenna, and the other two to fit the RT/duroid 6010 dielectric material. The final dimensions of the antenna are listed in Table 1. The variables in this Table refer to the notation used in Figs. 2 and 3.

Table 1: The dimensions of the final antenna element

Parameter	Value [mm]	Parameter	Value [mm]
Ws	24	Wfh	0.5
Ls	18	Wfv	1.6
L2	10.5	Wf	3.6
L3	7.7	G	0.8
L4	6.1	S	0.35
Wg	1	Ds	6.5
Lf	9.5	Hc	7.9
Sf	8.4	Hs	16.5
H	1.55	d	18.5
Thickness of superstrate	1.90	Width of superstrate	24
Length of superstrate	19		

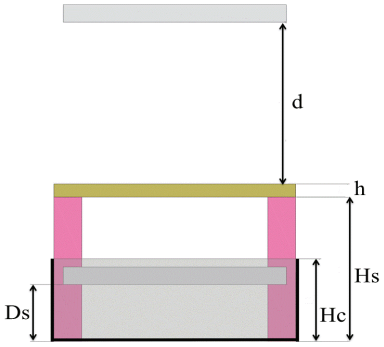

Fig. 2. Side view: brown horizontal rectangle represents the slot, two gray horizontal rectangles represent RT/duroid 6010 dielectric materials, two vertical purple rectangles represent styrofoam used for holding the cavity and the slot antenna together, and the black line represents the metallic cavity.

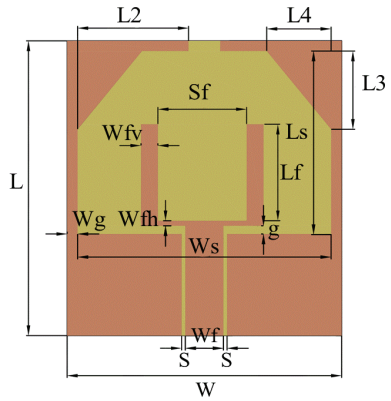

Fig. 3. Slot and feeding structure. (Note that after applying some modifications to this antenna, some of the geometrical parameters shown above are different than the original antenna presented in [16].)

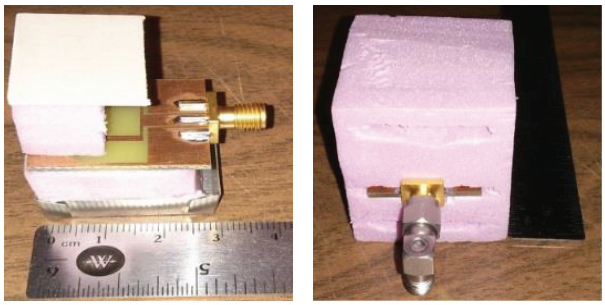

Fig. 4. [left] This demonstration model shows the superstrate on top of the slot antenna held with a piece of styrofoam, and the open metallic cavity placed beneath the antenna using a piece of styrofoam. The dielectric material placed between the cavity and the slot is not visible. [right] The final fabricated antenna is covered with the styrofoam box with three openings for the superstrate, slot antenna, and the dielectric between the slot and the cavity.

IV. SIMULATION AND MEASUREMENT RESULTS

Throughout this section, we refer to the monopole-like slot antenna with the metallic cavity and the two pieces of RT/duroid 6010 dielectric material as the "covered monopole-like slot antenna". We then refer to the same monopole-like slot antenna without the metallic cavity and without the two RT/duroid 6010 dielectric materials as the "monopole-like slot antenna". In both of these two antennas, the geometrical parameters of the slot and the fork-shaped feed are the same, and correspond to the modifications described in Section III, which has been listed in Table 1.

A. $|S_{11}|$ measurements

The simulated and measured $|S_{11}|$ of the covered monopole-like slot antenna are shown in Fig. 5. As can be seen in this figure, some of the impedance bandwidth of the original UWB monopole-like slot antenna, as reported in [16], has been sacrificed toward its evolution into the covered antenna. For MWT applications, we note that the impedance bandwidth requirement of $|S_{11}| \leq$ -10 dB might be too strict. Relaxing the definition of the impedance bandwidth to $|S_{11}| \leq$ -8 dB, the covered monopole-like slot antenna has the following impedance bandwidth of operation: 2.34 GHz to 5.04 GHz and 8.06 GHz to 13 GHz. Therefore, this covered monopole-like slot antenna can support multiple-frequency inversion. It should also be noted that these frequencies span a very wide range. Therefore, we speculate that it is more likely for this antenna to provide more independent information regarding the OI compared to another antenna that provides multiple frequencies of operation but within a limited range.

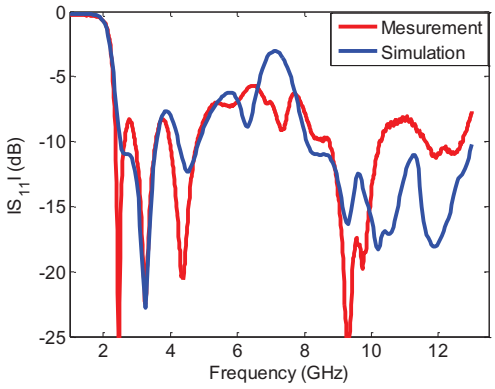

Fig. 5. Simulated and measured $|S_{11}|$ for the covered monopole-like slot antenna.

B. Near-field measurements

The near-field distributions of these two antennas were measured with a planar near-field range (PFNR). This PNFR, shown in Fig. 6, was manufactured by the Nearfield Systems Inc. (NSI). In this PNFR, the antenna under test (AUT) is stationary, and the measurement probe moves in front of the AUT to collect its near fields. The measurement probe is a WR90 open-ended waveguide probe with tapered ends. We had only access to an X-band (8.2 GHz- 12.4 GHz) probe. Thus, the near-field measurements are all performed in the X-band. In this PNFR, the probe is capable of sweeping a scan area with the size of 0.9×0.9 m^2 with a rectilinear data collection grid.

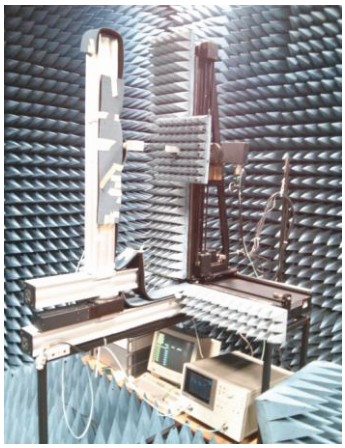

Fig. 6. Planar near-field range: the antenna backed with pyramidal absorbers is the open-ended waveguide probe. The other antenna is the covered monopole-like slot antenna under test. Absorbers have been taped on the tower that holds the antenna under test.

Based on the coordinate system shown in Fig. 1, the measurement plane will be in the *y*-*z* plane. Herein, for each of these two antennas we only show three sets of measurements, each of which corresponds to a specific distance (based on the coordinate system shown in Fig. 1, these distances are in the positive x direction from the AUT) from the slot to the measurement plane. These distances are 5 cm, 10 cm, and 14 cm. The size of the measurement plane for each of these distances is chosen in such a way that all these measurement planes will be within the same solid angle from the center of the antenna. (This solid angle represents a cone with the apex angle of 60º.) Therefore, the farther the measurement plane is from the antenna, the larger the measurement plane will be. For each of these measurement planes, we show the near-field data at three different frequencies within the X-band; namely, 8.6 GHz, 9 GHz, and 10 GHz.

For each set of measurements, the PNFR collects two components of the electric field at each point on the rectilinear grid of the measurement plane. Based on the coordinate system shown in Fig. 1, these two components of the electric fields are E_z and E_y, which are the tangential components of the electric fields on the measurement plane. It should be noted that, the PNFR is capable of performing these two electric field measurements due to its ability to rotate the probe 90º. Since the scope of this paper is 2D TM_z MWT, we only show the E_z measurements here. Also, to be able to compare different near-field measurement plots better, all the plots are normalized and the lower magnitude has been truncated to -10 dB.

As can be seen in Figs. 7 to 9, the covered monopole-like slot antenna creates a more focused beam in the measurement plane as compared to the monopole-like slot antenna. Also, a general trend that can be seen for both of these antennas is that the illumination area will become larger and larger as the distance of the probe from the antenna increases. Note that the number of near-field data points in the measurement planes corresponding to different distances are different due to the required sampling resolution in the PNFR.

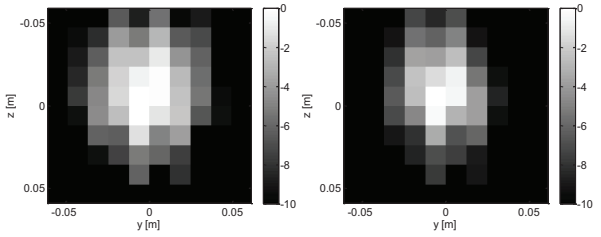

(a) 8.6 GHz (b) 8.6 GHz

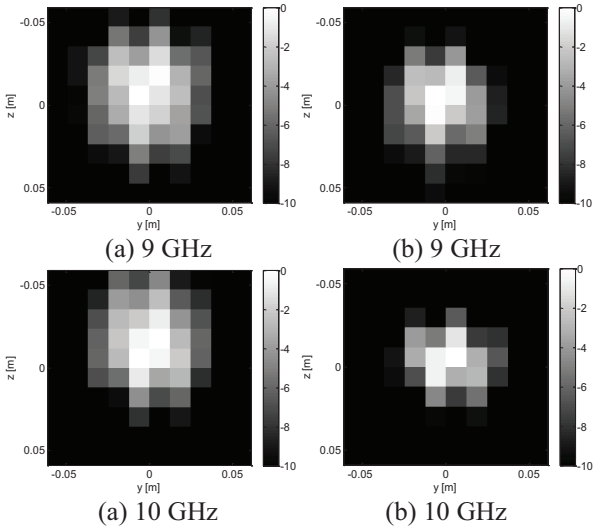

(a) 9 GHz (b) 9 GHz

(a) 10 GHz (b) 10 GHz

Fig. 7. [left] Monopole-like slot antenna, and [right] covered monopole-like slot antenna. The measured near-field E_z distribution of the antenna when the measurement plane is 5 cm away from the antenna at three different frequencies.

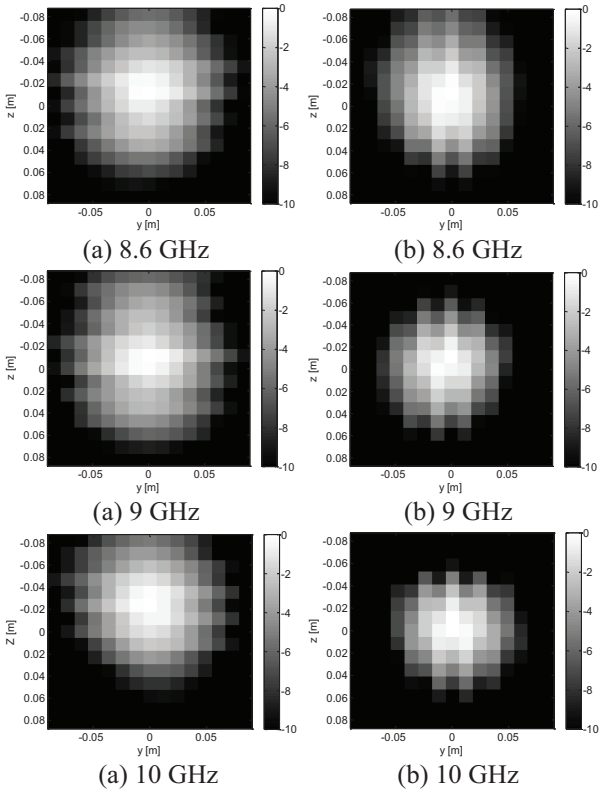

(a) 8.6 GHz (b) 8.6 GHz

(a) 9 GHz (b) 9 GHz

(a) 10 GHz (b) 10 GHz

Fig. 8. [left] Monopole-like slot antenna, and [right] covered monopole-like slot antenna. The measured near-field E_z distribution of the antenna when the measurement plane is 10 cm away from the antenna at three different frequencies.

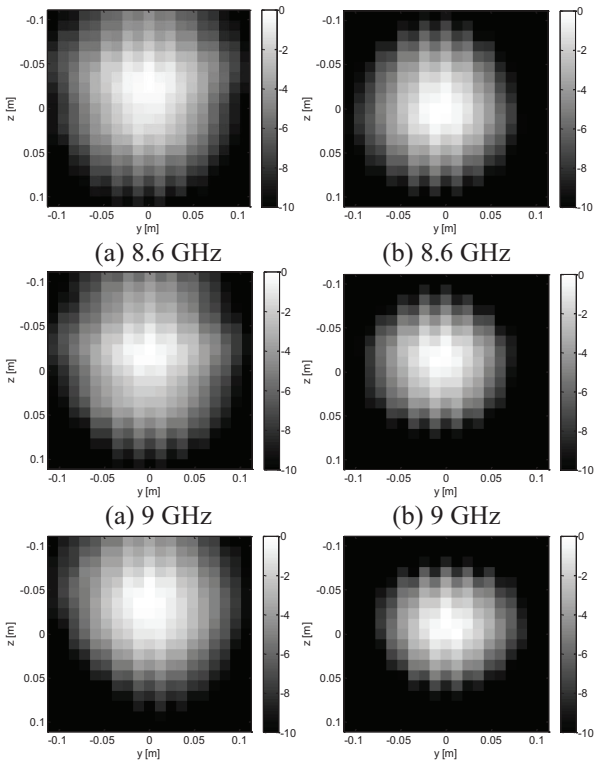

(a) 8.6 GHz (b) 8.6 GHz

(a) 9 GHz (b) 9 GHz

(a) 10 GHz (b) 10 GHz

Fig. 9. [left] Monopole-like slot antenna, and [right] covered monopole-like slot antenna. The measured near-field E_z distribution of the antenna when the measurement plane is 14 cm away from the antenna at three different frequencies.

Based on Fig. 7 to Fig. 9, we have shown that the covered monopole-like slot antenna has a more focused near-field distribution in the *y-z* plane as compared to the monopole-like slot antenna. This is important to satisfy our first requirement as noted in Section II. Now what remains is the measurement of the near-field of these two antennas in the imaging plane (*x-y* plane) for our third requirement as noted in Section II. However, this is not directly possible with the PNFR, as the PNFR is capable of performing measurements only in the *y-z* plane. Therefore, to this end, we measured the near-field data of each antenna at 23 different *y-z* planes starting from 5 cm away from the antenna to 16 cm with the step of 5 mm within the solid angle which has an apex of 60°. Having these 23 different sets of measurements, we can then extract the measurements that correspond to the points located on the *x-y* plane. However, since the spatial position of near-field data points can be different on each measurement plane, we used the *interpn* MATLAB function to interpolate these measurements into an identical sampling grid. Based on this approach, we were able to find the near-field data on the *x-y* plane. This measured near-field data at 9 GHz has been shown

in Fig. 10. As can be seen, the covered monopole-like slot antenna seems to have slightly more focused near-field beam in the *x-y* plane as compared to the monopole-like slot antenna. We note that the enhanced focusing is more clear in the measurement planes parallel to the *y-z* plane as compared to the plot in the *x-y* plane. This might be due to the fact that the chosen *x-y* plane has a smaller width (11 cm). This is in contrast to the *y-z* measurement planes whose width varies from about 11 cm to 20 cm. Note that, to obtain the near-field data over the *x-y* plane, we had to combine all these *y-z* near-field data. Therefore, the width of the resulting *x-y* near-field data will be the same as the smallest width in the *y-z* measurement planes. Also, it should be noted that the interpolation used to obtain the near-field data over the *x-y* plane might have some smoothing effects on the data, thus, not showing the focusing of the antenna sufficiently well.

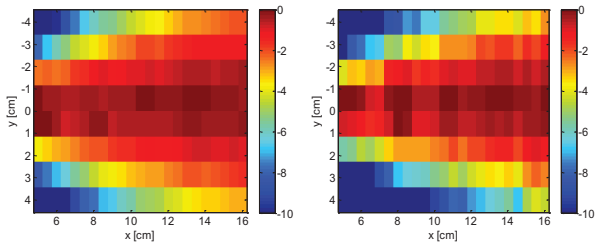

Fig. 10. Extracted measured near-field data over the *x-y* plane at 9 GHz for the two antennas: [left] monopole-like slot antenna, [right] covered monopole-like slot antenna

We also note that this extracted measured near-field data, as shown in Fig. 10, can be useful for the inversion algorithm. This can be understood by noting that inversion algorithms require the knowledge of the incident field data within the imaging domain. However, this incident field data is often not available; thus, inversion algorithms often assume some numerical model for the incident field distribution within the imaging domain, *e.g.*, a cylindrical Hankel function. Therefore, the use of such extracted near-field distributions can be helpful in reducing the modeling error. It should be noted that the fabricated antenna is a 3D structure, and therefore, cannot be entirely modeled within a 2D TM inversion algorithm.

We also investigated the near-field data over a larger *x-y* plane using the HFSS simulation. The *x-y* domain over which we chose to show this simulation is $x \in [0\ 20]$ cm and $y \in [-10\ 10]$ cm. Figures 11 and 12 show this simulation for two different frequencies: 4 GHz and 9 GHz. As expected, the covered monopole-like slot antenna creates a more focused near-field distribution in this domain. In summary, in this section, we have shown that the covered monopole-like slot antenna provides enhanced near-field focusing as compared to the monopole-like slot antenna in both the imaging plane and the plane perpendicular to the imaging plane.

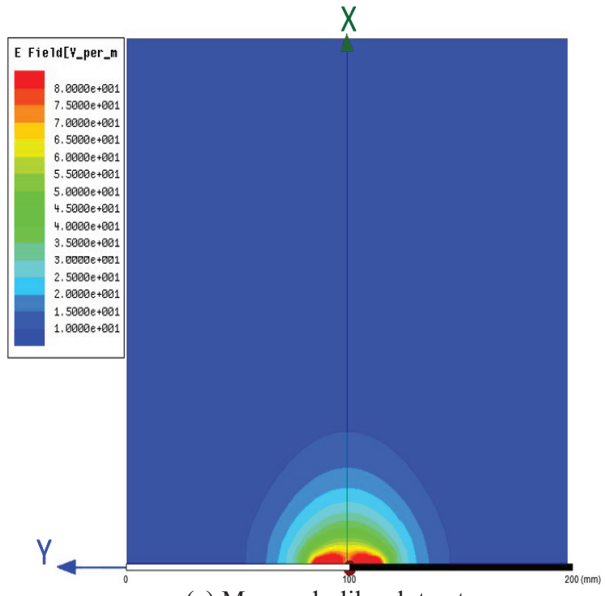

(a) Monopole-like slot antenna

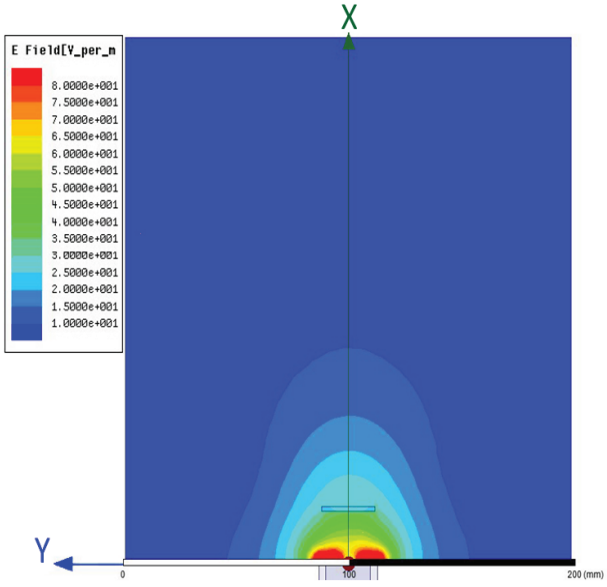

(b) Covered monopole-like slot antenna

Fig. 11. Simulated near-field data over the *x-y* plane at 4 GHz for the two antennas.

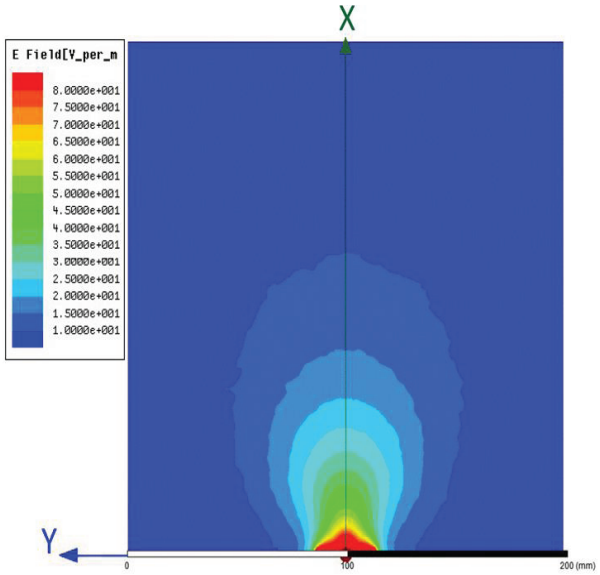

(a) Monopole-like slot antenna

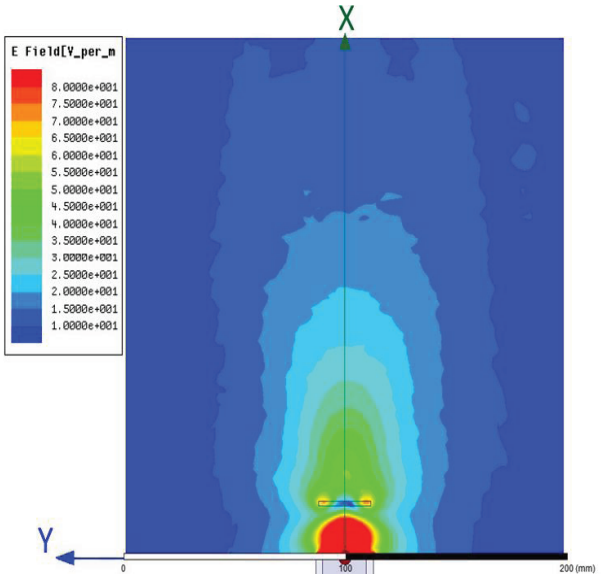

(b) Covered monopole-like slot antenna

Fig. 12. Simulated near-field data over the *x-y* plane at 9 GHz for the two antennas.

C. Electric field's vector components

The above results considered that component of the electric field that will be used for 2D TM$_z$ MWT; namely E_z component. As noted in Section II, it is desired to have E_x and E_y components of the vector electric field as small as possible in the imaging domain so as to reduce the modelling error associated with 2D TM inversion. Herein, using the HFSS simulations, we show the three components of the vector electric field on a semi-circle in front of the antenna in the *x-y* plane (imaging plane). This will be shown for two different radii, namely 7 cm and 10 cm, at two different frequencies, namely 9 GHz and 10 GHz. As can be seen in Figs. 13 and 14, the covered monopole-like slot antenna did not increase the magnitudes of E_x and E_y with respect to the desired component E_z as compared to the monopole-like slot antenna (maybe, except Fig. 14 (b)). In fact, as can be seen in these two figures, the covered antenna somehow improved the relative magnitude of E_z with respect to E_x and E_y.

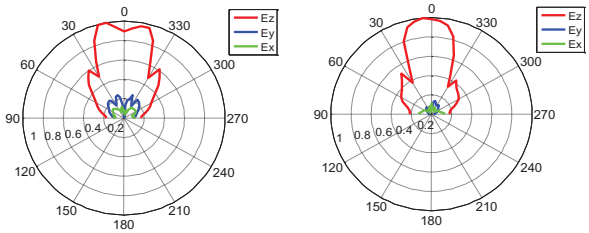

(a) Monopole-like slot (b) Covered monopole-like slot

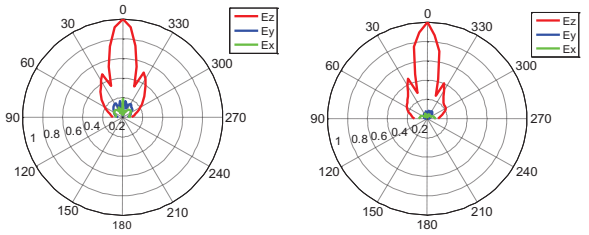

(c) Monopole-like slot (d) Covered monopole-like slot

Fig. 13. Simulation of the normalized magnitudes of the vector electric field components in the *x-y* plane at 9 GHz: (a)-(b) on a semi-circle of radius 7 cm, and (c)-(d) on a semi-circle of radius 10 cm.

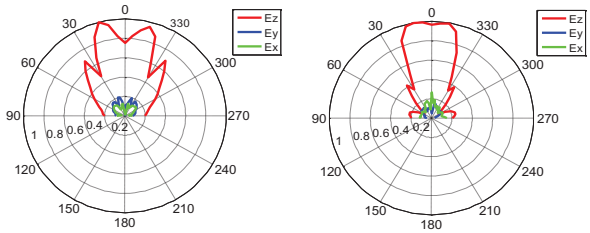

(a) Monopole-like slot (b) Covered monopole-like slot

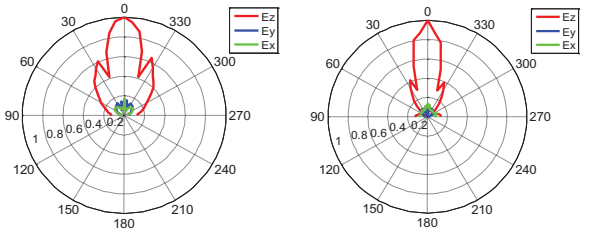

(c) Monopole-like slot (d) Covered monopole-like slot

Fig. 14. Simulation of the normalized magnitudes of the vector electric field components in the *x-y* plane (imaging plane) at 10 GHz: (a)-(b) on a semi-circle of radius 7 cm, and (c)-(d) on a semi-circle of radius 10 cm.

V. CONCLUSION

We presented and discussed some desired antenna specifications for performing 2D TM MWT so as to reduce the modeling error and enhance the achievable image accuracy. These desired specifications are near-field focusing in two orthogonal planes in the forward hemisphere of the antenna, reducing the backward radiation, making tangential electric field components on the imaging plane as small as possible, having multiple frequencies of operation and small size for the antenna, and the ability to model the antenna in the inversion algorithm. To this end, we have modified an existing antenna element. The modified antenna has been fabricated and tested in a PNFR. Through different experiments and simulations, it was shown that the modifications performed on this antenna were able to make its near-field distribution more focused, while maintaining multiple frequencies of operation, and keeping the antenna's physical size relatively small.

ACKNOWLEDGMENT

The financial support of the Natural Sciences and Engineering Research Council of Canada and the University of Manitoba's GETS is appreciated.

REFERENCES

[1] P. M. Meaney, M. W. Fanning, T. Raynolds, C. J. Fox, Q. Fang, C. A. Kogel, S. P. Poplack, and K. D. Paulsen, "Initial clinical experience with microwave breast imaging in women with normal mammography," *Acad Radiol*., 2007.

[2] S. Y. Semenov, R. H. Svenson, V. G. Posukh, A. G. Nazarov, Y. E. Sizov, A. E. Bulyshev, A. E. Souvorov, W. Chen, J. Kasell, and G. P. Tatsis, "Dielectrical spectroscopy of canine myocardium during acute ischemia and hypoxia at frequency spectrum from 100 KHz to 6 GHz," *IEEE Trans. Med. Imag*., vol. 21, no. 6, pp. 703-707, Jun. 2002.

[3] W. H. Weedon, W. C. Chew, and P. E. Mayes, "A step-frequency radar imaging system for microwave nondestructive evaluation," *Progress in Electromagnetic Research*, vol. 28, pp. 121-146, 2000.

[4] P. M. Meaney, K. D. Paulsen, J. T. Chang, M. W. Fanning, and A. Hartov, "Nonactive antenna compensation for fixed-array microwave imaging: part II-imaging results," *IEEE Trans. Med. Imag*., vol. 18, no. 6, pp. 508-518, 1999.

[5] T. Rubaek, P. M. Meaney, P. Meincke, and K. D. Paulsen, "Nonlinear microwave imaging for breast-cancer screening using Gauss-Newton's method and the CGLS inversion algorithm," *IEEE Trans. Antennas Propag.*, vol. 55, no. 8, pp. 2320-2331, Aug. 2007.

[6] S. Semenov, J. Kellam, Y. Sizov, A. Nazarov, T. Williams, B. Nair, A. Pavlovsky, V. Posukh, and M. Quinn, "Microwave tomography of extremities: 1. dedicated 2D system and physiological signatures," *Phys. Med. Biol*., vol. 56, pp. 2005-2017, 2011.

[7] C. Gilmore, P. Mojabi, A. Zakaria, M. Ostadrahimi, C. Kaye, S. Noghanian, L. Shafai, S. Pistorious, and J. LoVetri, "A wideband microwave tomography system with a novel frequency selection procedure," *IEEE Trans. Biomed. Eng*., vol. 57, no. 4, pp. 894-904, 2010.

[8] N. Bayat, *On the Role of Antennas in the Achievable Resolution and Accuracy from Near-Field Microwave Tomography*, M.Sc. thesis, University of Manitoba, Canada, 2014.

[9] N. Bayat and P. Mojabi, "An antenna element with improved near-field focusing for multiple-frequency microwave tomography applications," *IEEE APS and USNC-URSI Meeting*, Memephis, Tennessee, USA, Jul. 2014.

[10] C. Gilmore, *Towards an Improved Microwave Tomography System*, Ph.D. thesis, University of Manitoba, Canada, 2010.

[11] N. Bayat and P. Mojabi, "The effect of antenna incident field distribution on microwave tomography reconstruction," *Progress In Electromagnetics Research*, vol. 145, pp. 153-161, Mar. 2014.

[12] N. Bayat and P. Mojabi, "A mathematical framework to analyze the achievable resolution from microwave tomography," submitted, 2014.

[13] J. D. Shea, P. Kosmas, S. C. Hagness, and B. D. Van Veen "Three-dimensional microwave imaging of realistic numerical breast phantoms via a multiple-frequency inverse scattering technique," *Medical Physics*, vol. 37, no. 8, pp. 4210-4226, 2010.

[14] J. P. Stang, *A 3D Active Microwave Imaging System for Breast Cancer Screening*, Ph.D. dissertation, Duke University, Durham, USA, 2008.

[15] P. Mojabi and J. LoVetri, "A novel microwave tomography system using a rotatable conductive enclosure," *IEEE Trans. Antennas Propag*., vol. 59, no. 5, pp. 1597-1605, 2011.

[16] X. Qing and Z. N. Chen, "Compact coplanar waveguide-fed ultra-wideband monopole-like slot antenna," *Microwaves, Antennas Propagation, IET*, vol. 3, pp. 889-898, 2009.

[17] X. Qing and Z. N. Chen, "A miniaturized directional UWB antenna," *IEEE APS*, pp. 1470-147, Spokane, Washington, USA, Jul. 2011.

[18] J. Bourqui, M. Okoniewski, and E. Fear, "Balanced antipodal Vivaldi antenna with dielectric director for near-field microwave imaging," *IEEE Trans. Antennas Propag*., vol. 58, no. 7, pp. 2318-2326. Jul. 2010.

Nozhan Bayat received his M.Sc. degree in Electrical Engineering from the University of Manitoba, Canada, in 2014, where he is currently working towards the Ph.D. degree in Electrical Engineering. Bayat is a recipient of two international awards; namely, 2014 IEEE Antennas and Propagation Society (AP-S) Pre-Doctoral Research Award (awarded up to six students worldwide), and 2014 Antenna Measurement Techniques Association (AMTA) Student Travel Scholarship (awarded to one student worldwide). Bayat also received the Edward R. Toporek Graduate Fellowship in Engineering from Faculty of Engineering at the University of Manitoba in 2015. He is also a 2015 recipient of the University of Manitoba Graduate Fellowship for his doctoral studies. Bayat has also received an Outstanding Achievement Recognition Award in the Graduate Student Conference (GradCon) of the University of Manitoba's Department of Electrical and Computer Engineering in 2013.

Puyan Mojabi received his B.Sc. degree in Electrical Engineering from the University of Tehran, Iran, in 2002, M.Sc. degree in Electrical Engineering from Iran University of Science and Technology, Iran, in 2004 and Ph.D. degree in Electrical Engineering from the University of Manitoba, Canada, in 2010. He is currently an Assistant Professor with the Electrical and Computer Engineering Department at the University of Manitoba. Mojabi is a recipient of two Young Scientist Awards from the International Union of Radio Science (URSI) in 2014 (GASS) and 2015 (AT-RASC), and two student conference paper awards from the Applied Computational Electromagnetic Society (ACES) in 2007 and the Canadian National Committee of the URSI in 2008. He is also a recipient of the 2014 Excellence in Teaching Award from the Faculty of Engineering at the University of Manitoba. Mojabi is the elected Early Career Representative of URSI's Commission K. He also serves as the national representative of Commission E of the Canadian National Committee of URSI, and is also the current chair of the IEEE Winnipeg Section.